



Shocks in the Outflow of the RS Oph 2021 Eruption Observed with X-Ray Gratings

Marina Orío^{1,2}, E. Behar³, G. J. M. Luna^{4,5,6}, J. J. Drake⁷, J. Gallagher¹, J. S. Nichols⁷, J. U. Ness⁸, A. Dobrotka⁹,
J. Mikołajewska¹⁰, M. Della Valle^{11,12}, R. Ignace¹³, and R. Rahin³

¹ Department of Astronomy, University of Wisconsin, 475 N. Charter Str., Madison, WI 53706, USA; orio@astro.wisc.edu

² INAF-Padova, vicolo Osservatorio 5, I-35122 Padova, Italy

³ Department of Physics, Technion, 32000 Haifa, Israel

⁴ CONICET-Universidad de Buenos Aires, Instituto de Astronomía y Física del Espacio (IAFE), Av. Inte. Güiraldes 2620, C1428ZAA, Buenos Aires, Argentina

⁵ Universidad de Buenos Aires, Facultad de Ciencias Exactas y Naturales, Buenos Aires, Argentina

⁶ Universidad Nacional de Hurlingham, Av. Gdor. Vergara 2222, Villa Tesei, Buenos Aires, Argentina

⁷ Harvard & Smithsonian Center for Astrophysics, 60 Garden Street, Cambridge, MA 02138, USA

⁸ European Space Agency (ESA), European Space Astronomy Centre (ESAC), Camino Bajo del Castillo s/n, E-28692 Villanueva de la Cañada, Madrid, Spain

⁹ Advanced Technologies Research Institute, Faculty of Materials Science and Technology in Trnava, Slovak University of Technology in Bratislava, Bottova 25, 917 24 Trnava, Slovakia

¹⁰ Nicolaus Copernicus Astronomical Center, Polish Academy of Sciences, Bartycka 18, 00716 Warsaw, Poland

¹¹ Capodimonte Astronomical Observatory, INAF-Napoli, Salita Moiariello 16, I-80131, Napoli, Italy

¹² ICRANet, Piazza della Repubblica 10, I-65122 Pescara, Italy

¹³ Physics & Astronomy, East Tennessee State University, Johnson City, TN 37615, USA

Received 2022 August 8; revised 2022 September 2; accepted 2022 September 2; published 2022 October 12

Abstract

The 2021 outburst of the symbiotic recurrent nova RS Oph was observed with the Chandra High Energy Transmission Gratings (HETG) on day 18 after optical maximum and with XMM-Newton and its Reflection Grating Spectrographs (RGS) on day 21, before the supersoft X-ray source emerged and when the emission was due to shocked ejecta. The absorbed flux in the HETG 1.3–31 Å range was 2.6×10^{-10} erg cm⁻² s⁻¹, three orders of magnitude lower than the γ -ray flux measured on the same date. The spectra are well fitted with two components of thermal plasma in collisional ionization equilibrium, one at a temperature $\simeq 0.75$ keV and the other at a temperature in the 2.5–3.4 keV range. With the RGS we measured an average flux of 1.53×10^{-10} erg cm⁻² s⁻¹ in the 5–35 Å range, but the flux in the continuum and especially in the lines in the 23–35 Å range decreased during the 50 ks RGS exposure by almost 10%, indicating short-term variability on a timescale of hours. The RGS spectrum can be fitted with three thermal components, respectively at plasma temperatures between 70 and 150 eV, 0.64 keV, and 2.4 keV. The post-maximum epochs of the exposures fall between those of two grating spectra observed in the 2006 eruption on days 14 and 26: they are consistent with a similar spectral evolution, but in 2021 cooling seems to have been more rapid. Iron is depleted in the ejecta with respect to solar values, while nitrogen is enhanced.

Unified Astronomy Thesaurus concepts: [Classical novae \(251\)](#)

1. Introduction

RS Oph is arguably the best known recurrent symbiotic nova. Classical and recurrent novae are binary systems hosting a white dwarf (WD), and their outbursts are attributed to a thermonuclear runaway (TNR) on the surface of the WD, which is accreting material from its binary companion. The TNR is usually followed by a radiation-driven wind, which depletes the accreted envelope (Starrfield et al. 2012; Wolf et al. 2013). The designation “recurrent” implies that the outburst is observed more than once in a human lifetime, although all novae (including the *classical*) are thought to be recurrent, on secular timescales that can vary greatly, depending on the mass accretion rate and the WD mass. The more massive the WD is, the smaller its radius, so the accumulated material is more degenerate and is ignited with lower accreted mass (Yaron et al. 2005; Starrfield et al. 2012; Wolf et al. 2013). Thus, the frequently erupting recurrent novae host rather massive WDs. RS Oph is also a symbiotic system, that is a system with a red giant companion, specifically an

M0–2 III mass donor (Dobrzycka et al. 1996; Anupama & Mikołajewska 1999) in a binary with a 453.6 day orbital period (Brandi et al. 2009). Brandi et al. (2009) and Mikołajewska & Shara (2017) presented compelling evidence that the WD is very massive, in the 1.2–1.4 M_{\odot} range, and that it is a carbon–oxygen WD. The effective temperature estimated in the supersoft X-ray phase by Nelson et al. (2008) in 2006 was about 800,000 K, which is indicative of a mass of at least 1.2 M_{\odot} . This implies that it must have grown in mass and not have ejected all the accreted material, since calculations indicate that the mass of newly formed WDs is $< 1.2 M_{\odot}$, and in most models does not exceed 1.1 M_{\odot} (see, among others, Meng et al. 2008). Such a high CO WD mass has spurred much interest in the possibility that RS Oph is a Type Ia supernova progenitor. RS Oph was observed in outburst in 1898, 1933, 1958, 1967, 1985, and 2006. Two additional outbursts may have been missed in 1907 and 1945 when RS Oph was aligned with the Sun (Schaefer 2004).

Novae are luminous at all wavelengths from gamma rays to radio, and X-rays have proven to be a very important window to understanding their physics since the 1980s (Oegelman et al. 1984). After the thermonuclear flash, the WD atmosphere contracts and returns almost to pre-outburst radius. The peak wavelength of the emission moves from the optical range to the



Original content from this work may be used under the terms of the [Creative Commons Attribution 4.0 licence](#). Any further distribution of this work must maintain attribution to the author(s) and the title of the work, journal citation and DOI.

UV and extreme UV and finally to soft X-rays within a short time, in a phase of constant bolometric luminosity, still powered by shell burning. The central source appears as a supersoft X-ray source, with peak temperature up to a million kelvin, for a time lasting from days to a few years (Orio 2012). The first outburst that could be monitored in X-rays was the one of 2006, with Swift and RXTE (Bode et al. 2006; Hachisu et al. 2007; Osborne et al. 2011; Sokoloski et al. 2006), and with high spectral resolution with the gratings of Chandra and XMM-Newton (Ness et al. 2007, 2009; Nelson et al. 2008; Drake et al. 2009). In outburst, RS Oph is one the most luminous novae in X-rays, even though several novae have been observed by now much closer to us. The distance inferred from the expansion velocity and resolved radio imaging of 2006 is 2.45 ± 0.37 kpc (Rupen et al. 2008). Assuming that the giant fills its Roche lobe, and using the orbital parameters of Brandi et al. (2009), the resulting distance is 3.1 ± 0.5 kpc (Barry et al. 2008). Finally, the GAIA DR-3 distance is $2.44^{+0.08}_{-0.16}$ kpc (geometric) and $2.44^{+0.21}_{-0.22}$ kpc (photogeometric) (see Bailer-Jones et al. 2021). The uncertainty on the GAIA parallax may be larger than estimated, because of difficulties arising from the surrounding nebula and the wobble of the long binary period; however, the derived distance range is in good agreement with the most recent and updated measurements. Some of the older estimates of the distance to RS Oph are no longer relevant now, since the binary parameters are better known. We note that many papers in the past adopted the 1987 estimate of 1.6 kpc based on the intervening neutral hydrogen column density to the source (Bode 1987; Hjellming et al. 1986).

RS Oph’s latest outburst was observed on 2021 August 9 at 22:20 UT (as announced in <http://ooruri.kusastro.kyoto-u.ac.jp/mailarchive/vsnet-alert/26131> and <http://www.cbat.eps.harvard.edu/iau/cbet/005000/CBET005013.txt>) at visual magnitude 4.8. Immediately afterwards, the nova was also detected at gamma-ray energy with the Fermi-LAT (Cheung et al. 2022), H.E.S.S. (Wagner & H.E.S.S. Collaboration 2021a, 2021b; H.E.S.S. Collaboration 2022), and MAGIC (Acciari et al. 2022), and in hard X-rays with MAXI (Shidatsu et al. 2021) and INTEGRAL (Ferrigno et al. 2021). The highest energy range was that of H.E.S.S. and MAGIC, from 10 GeV to tens of TeV, and the flux peaked in its “softest” range, with a power-law index >3 , significantly higher than the power-law index of 1.9 in the spectrum measured with the Fermi-LAT in the 100 MeV–13 GeV range.

The early optical spectrum was described by Munari & Valisa (2021a) as of “He/N” type, with strong Balmer, He I, and N II lines. The emission lines had full width at half maximum of 2900 km s^{-1} and blueshifted P-Cyg components, which disappeared within a few days (Mikolajewska et al. 2021; Munari et al. 2021). Acceleration to up to $\simeq 4700 \text{ km s}^{-1}$ was observed after the first two days, and P-Cyg profiles appeared also in lines of Fe II, O I, and Mg II (Mikolajewska et al. 2021; Pandey et al. 2022). A narrow emission component disappeared within the first few days, while a narrow absorption component persisted for longer (Luna et al. 2021; Shore et al. 2021), and altogether the velocity of the lines indicated deceleration (Munari et al. 2021) a few days after the initial acceleration. Intrinsic linear optical polarization was observed ~ 1.9 days after outburst (Nikolov & Luna 2021), while satellite components appeared in the optical spectra after two weeks in H α and H β , suggesting a bipolar outflow as

observed in the radio in 2006 (Rupen et al. 2008). High ionization lines appeared around day 18 of the outburst (Shore et al. 2021). A summary and visual illustration of the optical spectral changes in the first three weeks after maximum can be found in Munari & Valisa (2021b) and Pandey et al. (2022).

The AAVSO optical light curve of RS Oph in different bands, from *B* to *I*, in 2021 appeared extremely similar to the AAVSO 2006 light curve. The maximum magnitude was $V = 4.8$, the time for a decay by 2 mag, t_2 , was 7 days and the time for a decay by 3 mag, t_3 , was 14 days. All the subsequent evolution was smooth, and in the last optical observations on 2021 November 14 the nova was at $V \simeq 11.2$, like in 2006 at the same post-outburst epoch. However, the X-ray light curve was quite different from the 2006 one, with a shorter and less luminous supersoft X-ray phase (Page et al. 2022; M. Orio et al. 2022, in preparation on NICER monitoring).

Here we analyze and discuss high-resolution X-ray spectroscopy obtained with the Chandra HETG on 2021 August 27 and with the XMM-Newton RGS on 2021 August 30. Section 2 describes the Chandra spectrum, model fitting, and line profiles and fluxes. Section 3 describes the XMM-Newton spectra and light curves, again with spectral fits and line fluxes and profiles. Section 4 describes a comparison with observations made during the 2006 outburst. Section 5 is dedicated to a discussion of our findings, and conclusions are in Section 6.

2. The Chandra Observation

The high energy grating (HEG) and medium energy grating (MEG) were coupled with the ACIS-S detector, and spectra were obtained on 2021 August 27 in a 20 ks long exposure starting at 00:56:43. We extracted these spectra with the CIAO software (Fruscione et al. 2006) version 4.14.0 and the CALDB calibration package version 4.9.7. Both the HEG and MEG were used, with respective absolute wavelength accuracies of 0.0006 \AA and 0.011 \AA . We measured a count rate of $0.444 \pm 0.004 \text{ counts s}^{-1}$ in the zeroth-order ACIS-S camera (with an estimated pile-up fraction of about 10%). We extracted the ACIS-S light curve and found no significant variability during the exposure.

Half of the incident radiation is dispersed to the gratings in this observation mode, and the count rates were $1.622 \pm 0.010 \text{ counts s}^{-1}$ in the HEG $+1/-1$ orders (energy range 0.8–10 keV, wavelength range 1.2–15 \AA), and $1.271 \pm 0.013 \text{ counts s}^{-1}$ in the MEG summed $+1/-1$ orders (energy range 0.4–5 keV, wavelength range 2.5–31 \AA). The integrated fluxes in the two instruments were measured as $2.367 \times 10^{-10} \text{ erg cm}^{-2} \text{ s}^{-1}$ in the HEG and $2.605 \times 10^{-10} \text{ erg cm}^{-2} \text{ s}^{-1}$ in the MEG. The HEG and MEG spectra, shown in Figure 1, are rich in prominent emission lines due to H-like and He-like transitions, from calcium to neon.

2.1. Model Fitting to the HETG Spectra

Spectral fitting was done with the HEASOFT XSPEC tool, version 6.30.1, after the data were binned by signal-to-noise ratio with the GRPPHA tool (see Dorman & Arnaud 2001, and references therein).

Figure 1 shows in red the best fit with a two-component BVAPEC model in XSPEC, of thermal plasma in collisional ionization equilibrium with line broadening and variable abundances, and a TBABS model of absorbing column density.

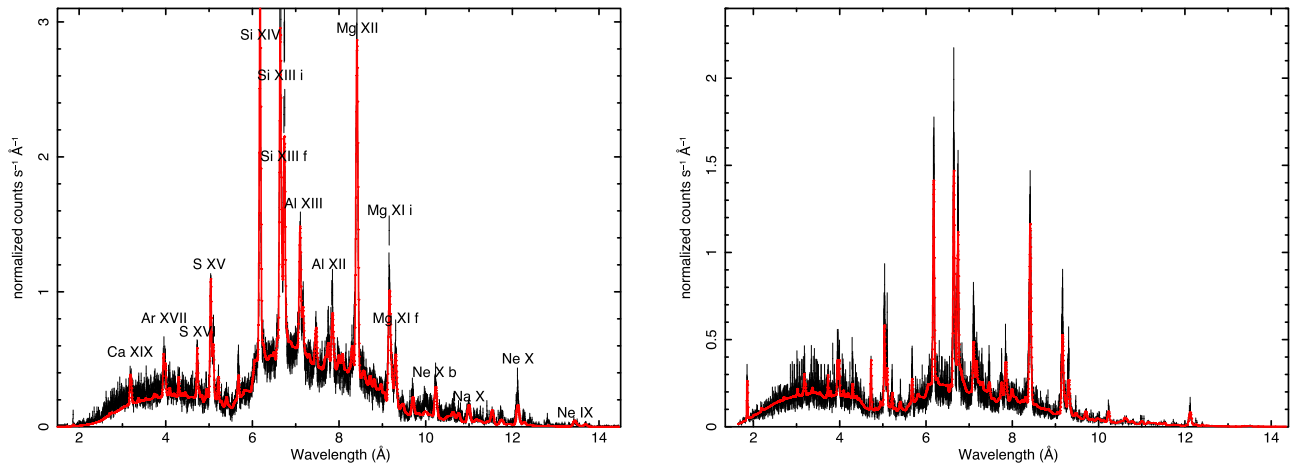


Figure 1. The spectrum observed with the Chandra MEG grating (left) and with the Chandra HEG grating (right) on 2021 August 27, day 18 after optical maximum, and a fit with the two APEC components described in the text, whose parameters are given in the second column of Table 1.

With χ^2 statistics, which we found to be appropriate in this case, we obtained a value of χ^2 per degree of freedom ($\chi^2/\text{d.o.f.}$) of about 1. The parameters of the fits are given in Table 1. In addition to the line broadening, the global fit is improved by allowing a blueshift as a free parameter. This blueshift velocity necessary in the fit is modest with respect to typical nova wind velocity, only 264 km s^{-1} , and in previous X-ray observations of novae it has been explained as an apparent effect of differential absorption, eroding the red wing of each line more than the blue wing because material moving toward us is absorbed by fewer layers of intrinsic absorbing material than the receding outflow (Ignace 2001; Orlando et al. 2009, 2017; Drake et al. 2009, 2016; Orio et al. 2020). We explore this effect more in the next section.

We allowed the abundances of elements from neon to iron that have many transitions in the observed energy range (specifically Ne, Mg, Al, Si, S, Ar, Ca, and Fe) to be free parameters, but, in order to reduce the number of free parameters, we assumed these abundances to be the same in the two components, although this may not be so (see models by Orlando et al. 2009).

Figure 2 shows two of the He-like triplets observed with the HEG, namely the prominent Si XIII and S XV lines. With a Gaussian fit to the lines, for Si XIII we found that the G -ratio of the sum of the fluxes in the intercombination and forbidden lines to the flux in the resonance line, indicated as $G = (i + f)/r$, is 1.26 ± 0.12 for S XV, 0.82 ± 0.10 for Si XIII, and 0.77 ± 0.18 for Mg XI (see Table 2).

As long as the forbidden line is formed in a certain electron density range, which depends on the specific element, a value $G < 4$ indicates that the contribution of photoionization is not important (Porquet et al. 2010). We discuss line profiles and fluxes more in detail in the next section, in which we also analyze diagnostics of electron density. Figure 3 (where only the model is plotted) shows the respective contributions of the two thermal components in the model to the continuum, H-like and He-like lines. While both components contribute in the same way to the continuum and quite similarly to the H-like lines at shorter wavelengths, the hot component contributes increasingly less to H-like lines formed at lower energy. Moreover, it turns out that the gas of the hotter component is close to being fully ionized, so its contribution to the He-like lines is negligible.

Table 1
Parameters for the Two HETG Models Described in the Text, Both with Two BVAPEC Components

| | $N(\text{H})$ Free | $N(\text{H})$ Fixed |
|---|------------------------------------|------------------------------------|
| $\chi^2/\text{d.o.f.}$ | 1.0 | 1.1 |
| $N(\text{H}) \times 10^{21} \text{ cm}^{-2}$ | 10.3 ± 0.4 | 5.2 |
| kT_1 (keV) | 0.76 ± 0.01 | 0.77 ± 0.12 |
| kT_2 (keV) | 2.83 ± 0.25 | 3.58 ± 0.11 |
| $\text{EM}_1 \times (d(\text{kpc})/2.4)^2$ | $(2.835 \pm 0.105) \times 10^{58}$ | $(1.366 \pm 0.038) \times 10^{58}$ |
| $\text{EM}_2 \times (d(\text{kpc})/2.4)^2$ | $(1.574 \pm 0.091) \times 10^{58}$ | $(1.428 \pm 0.033) \times 10^{58}$ |
| $F_{a,\text{tot}} \times 10^{-10} \text{ erg cm}^{-2} \text{ s}^{-1}$ | 2.63 ± 0.15 | 2.78 ± 0.07 |
| $F_{a,1} \times 10^{-10} \text{ erg cm}^{-2} \text{ s}^{-1}$ | 1.00 ± 0.04 | 0.84 ± 0.02 |
| $F_{a,2} \times 10^{-10} \text{ erg cm}^{-2} \text{ s}^{-1}$ | 1.63 ± 0.09 | 1.94 ± 0.05 |
| $F_{\text{un}} \times 10^{-9} \text{ erg cm}^{-2} \text{ s}^{-1}$ | 1.05 ± 0.06 | 0.58 ± 0.03 |
| $\text{Ne}/\text{Ne}_\odot$ | 1.15 ± 0.11 | 0.77 ± 0.07 |
| $\text{Mg}/\text{Mg}_\odot$ | 1.02 ± 0.04 | 1.21 ± 0.05 |
| $\text{Al}/\text{Al}_\odot$ | 0.92 ± 0.11 | 1.39 ± 0.15 |
| $\text{Si}/\text{Si}_\odot$ | 0.75 ± 0.03 | 1.16 ± 0.05 |
| S/S_\odot | 0.98 ± 0.06 | 1.58 ± 0.08 |
| $\text{Ar}/\text{Ar}_\odot$ | 0.93 ± 0.12 | 1.23 ± 0.18 |
| $\text{Ca}/\text{Ca}_\odot$ | 0.62 ± 0.15 | 0.61 ± 0.20 |
| $\text{Fe}/\text{Fe}_\odot$ | 0.28 ± 0.03 | 0.07 ± 0.02 |
| v_{bs} (km s^{-1}) | 265 ± 13 | 264 ± 13 |
| v_{br} (km s^{-1}) | 677 ± 14 | 680 ± 14 |

Note. The emission measure (EM) is the integral over the emitting volume of the electron density multiplied by the ion density. Electron and ion densities are assumed to be equal, so that, to a first approximation, $\text{EM} = V \times n_e^2$. The values are normalized assuming a distance of 2.4 kpc. Abundances of elements with relevant emission lines are also given, and so are the blueshift and broadening velocity. The statistical uncertainty listed is the larger of the positive and negative 90% confidence levels.

In Table 1 we give the 90% confidence level error for each free parameter obtained by assuming the other parameters are fixed. We also analyzed the confidence contours obtained by varying two parameters simultaneously. We found that the temperature of the softer components varies in a narrow range ($0.72\text{--}0.78 \text{ keV}$ within a 2σ uncertainty) if we let either $N(\text{H})$ or the temperature of the other component vary. The column

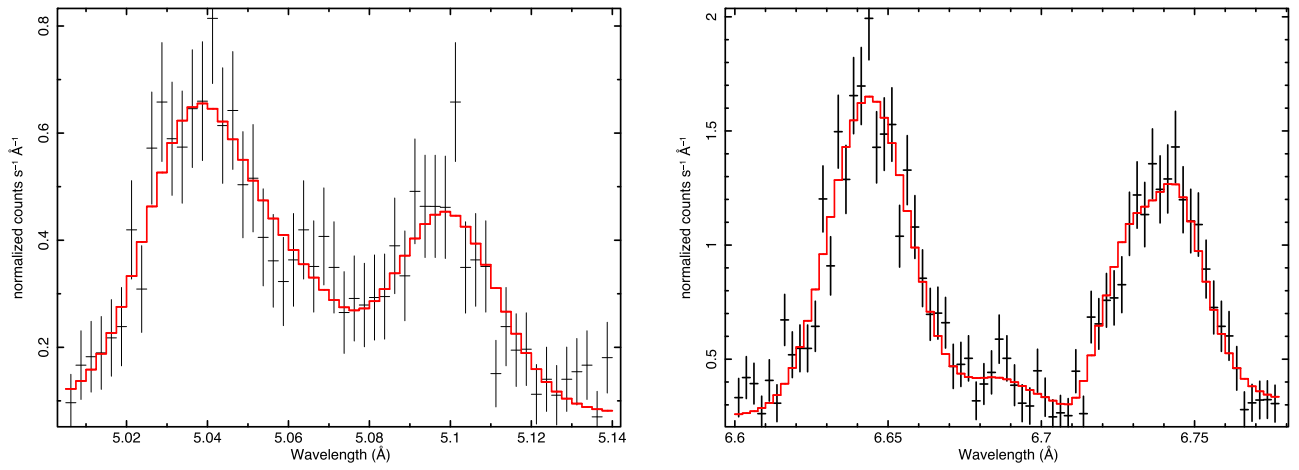


Figure 2. The observed profile, in the count rate spectrum, of the Si XIII (right) and S XV (left) He-like triplets observed with the HEG. The clear line on the left with the highest count rate is the resonance (r), the clear line on the right is the forbidden (f), while in the middle an intercombination (i) line is barely resolved. The i line is composed of two lines very close in wavelength, hardly resolvable. The red lines show the fits with three Gaussians with the same width, and a locally evaluated underlying continuum, convolved with the instrumental response.

Table 2
Line Measurements for the HEG and MEG Spectrum

| Ion | Grating | λ_0 (Å) | λ (Å) | F_x (10^{-12} erg cm $^{-2}$ s $^{-1}$) | σ (km s $^{-1}$) |
|-----------|---------|------------------|--------------------|---|--------------------------|
| Fe XXVI | HEG | 1.850–1.868 | 1.859 (fixed) | 3.961 ± 0.780 | |
| S XVI | MEG | 4.7273 | 4.725 ± 0.003 | $1.333^{+1.340}_{-0.255}$ | 1016 ± 400 |
| S XV—r | HEG | 5.0387 | 5.038 ± 0.003 | 3.006 ± 0.451 | 289 ± 30 |
| S XV—i | | 5.0631, 5.0616 | 5.068 ± 0.002 | 1.326 ± 0.351 | |
| S XV—f | | 5.102 | 5.099 ± 0.0045 | 2.462 ± 0.391 | |
| Si XIV | HEG | 6.180–6.186 | 6.179 ± 0.003 | 3.530 ± 0.247 | 146 ± 15 |
| | RGS | | 6.177 ± 0.004 | 3.217 ± 1.220 | 194 ± 20 |
| Si XIII—r | HEG | 6.648 | 6.644 ± 0.002 | 4.661 ± 0.261 | 267 ± 15 |
| | RGS | | 6.640 | 4.562 | 1174 ± 633 |
| Si XIII—i | | 6.685, 6.688 | 6.684 ± 0.006 | 0.716 ± 0.035 | |
| | RGS | | 6.633 ((fixed)) | 0.938 ± 0.094 | |
| Si XIII—f | | 6.7403 | 6.735 ± 0.001 | 3.095 ± 0.217 | |
| | RGS | | 6.723 (fixed) | 3.769 ± 0.754 | |
| Mg XII | HEG | 8.419 | 8.411 ± 0.003 | 4.172 ± 0.350 | 463 ± 0.48 |
| | RGS | | 8.405 ± 0.004 | 5.153 ± 0.234 | 999 ± 131 |
| Mg XI—r | MEG | 9.169 | 9.157 ± 0.028 | 2.764 ± 0.195 | 688 ± 48 |
| | RGS | | 9.156 | 3.387 ± 0.256 | 2588 ± 439 |
| Mg XI—i | MEG | 9.228, 9.231 | 9.219 ± 0.004 | 0.798 ± 0.123 | |
| | RGS | | 9.205 (fixed) | 0.964 ± 0.193 | |
| Mg XI—f | MEG | 9.314 | 9.306 ± 0.004 | 1.337 ± 0.078 | |
| | RGS | | 9.294 | 1.975 ± 0.197 | |
| Ne X | MEG | 12.132 (12.138) | 12.120 (fixed) | 2.068 ± 0.168 | 445 ± 67 |
| | RGS | 12.132 (12.138) | 12.112 ± 4 | 3.999 ± 0.299 | 1804 ± 170 |
| Fe XVII | RGS | 15.031 | 15.001 (fixed) | 1.669 ± 0.073 | 480 ± 53 |
| Fe XVII | RGS | 15.261 | 15.232 ± 0.024 | 4.874 ± 0.561 | |
| Fe XVIII? | RGS | 15.232 | 15.157 (fixed) | 0.226 ± 0.043 | |
| N VII | RGS | 24.779, 24.785 | 24.716 ± 0.005 | 1.269 ± 0.040 | 956 ± 37 |
| N VI—r | RGS | 28.780 | 28.760 ± 0.009 | 4.077 ± 0.068 | 1313 |
| N VI—i | RGS | 28.0819, 29.0843 | 29.084 ± 0.499 | 0.298 ± 0.021 | |
| N VI—f | RGS | 29.5346 | 29.449 ± 0.016 | 1.416 ± 0.014 | |

Note. The MEG was used for the S XVI, Ne XI, and Mg XI lines, the HEG for the rest. The whole Fe XXVI triplet was treated as one Gaussian to estimate the flux, because of resolution difficulties. “fixed” means that the Gaussian center was evaluated by eye instead of being a free parameter. The Gaussian width of the triplets was assumed to be the same for the r, i, and f lines. The uncertainty reported in the table is the larger of the 90% statistical errors in the + and – directions.

density $N(\text{H})$ and the temperature of the hotter component are less well constrained. T_2 is in the 2.45–3.45 keV range within 2σ .

In Table 1 we give both the parameters of the fit that yielded a reduced $\chi^2/\text{d.o.f.} \simeq 1$ that gave the best fit to the HETG alone, and the fit with $N(\text{H})$ constrained by fitting also the

spectrum obtained from a public NICER observation made on 2021 August 26 starting at 07:41:00, in an uninterrupted 2170 s exposure. With a joint fit, we obtained a best-fit value $N(\text{H}) = 5.2 \times 10^{21}$ cm $^{-2}$. This is still consistent with fitting the HETG spectrum alone, because the fits have different minima of the χ^2 parameter when we explore a large parameter

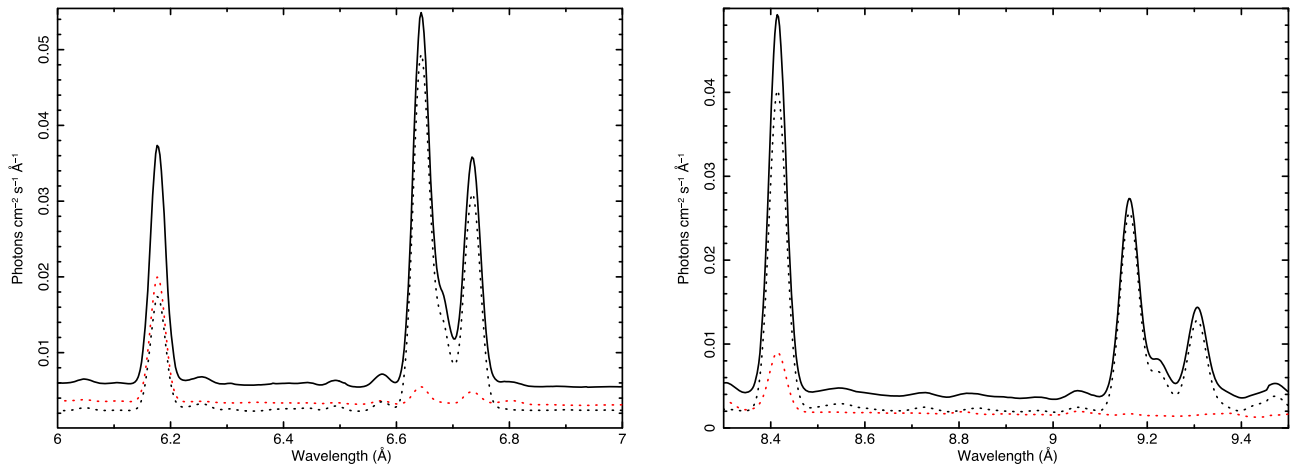


Figure 3. A close-up showing the model with two thermal components in Table 1 (middle column) and in Figure 1, resulting from fitting the binned spectrum with signal-to-noise ratio of 10 and convolving it with the instrument response for the Si XIV H-like, S XIII He-like, Mg XII H-like, and Mg XI He-like lines. The hotter component is shown in red, the less hot with the black dotted line, and the sum of the two with the black solid line. As shown also by Figure 2, the intercombination lines are predicted to be unresolvable, so we see only two clear lines (r and f) in the model.

space, even if the other parameters are constrained within quite narrow ranges. The NICER monitoring of RS Oph and its results are described in an accompanying paper (M. Orio et al. 2022, in preparation).

In the third column of Table 1 we also list the parameters of the fit to the HETG spectra when fixing the value of $N(\text{H})$ previously obtained and including NICER in the fit. Adding the NICER broadband spectrum constrained $N(\text{H})$ but introduced larger errors in the other parameters, so we show only the values obtained for the HETG, fixing the $N(\text{H})$ parameter. The new value of $N(\text{H})$, $5.2 \times 10^{21} \text{ cm}^{-2}$, differs by slightly more than 2σ from the value obtained with the HETG alone, but NICER is sensitive to energy as low as 0.2 keV, and we inferred that the NICER fit gives a more precise estimate of $N(\text{H})$. Fixing this $N(\text{H})$ value, we could still fit the HETG spectra with $\chi^2/\text{d.o.f.} \simeq 1.1$. Table 1 shows that with this $N(\text{H})$ value the HETG spectra are fitted with almost unvaried temperature of the cooler component, but with a higher temperature of the hotter one than in the “free $N(\text{H})$ ” fit. We reasoned that, while the absorption is better determined in the lower energy range of NICER, the temperatures of both components are much more reliably estimated with the HETG because they depend on line intensities and line ratios. Both model fits in Table 1 predict subsolar abundances of calcium and iron, moderately enhanced neon and magnesium, while the abundances of other elements are not well constrained: they are slightly enhanced in the fit with higher $N(\text{H})$ value and slightly depleted in the fit with $N(\text{H})$ value that also fits the NICER spectrum.

We tried a third fit, not shown in the table, without “tying” the abundances of the two components, namely assuming that the abundances are *not* the same in the two plasma components. With the fixed value of $N(\text{H})$ adopted in the third column of Table 1 and also with a free $N(\text{H})$ value, we obtained a value of $\chi^2/\text{d.o.f.} = 1$ with depleted iron, but almost solar abundances of elements from neon to calcium in the hotter component, and largely enhanced (>30 times solar) abundances in the less hot one. With the fixed value of $N(\text{H})$, in this model the best-fit temperatures are slightly different, 2.84 keV and 0.59 keV. The emission lines appear to be somewhat better fitted, but statistically the result is not preferred and it has too

many free parameters to constrain the abundances very significantly.

2.2. Line Profiles and Line Fluxes

Table 2 shows the measurements of all the lines that had a significant detection above the continuum, fitted with Gaussian profiles above a continuum that is estimated locally, in a narrow range around each line, with a power law. For the He-like triplets, we assumed that σ of the Gaussian (which we attribute to broadening velocity and as such is indicated in the table) is the same for the resonance, intercombination, and forbidden line. Figure 2 shows examples of this fit for Si XIII and S XIV. We also examined the line variability during the exposure by dividing the spectrum into six subintervals of equal duration, and did not measure significant variability in any line fluxes.

The fit with the two thermal components in Table 1 includes a blueshift velocity, corresponding to $\simeq 263 \pm 13 \text{ km s}^{-1}$, and line broadening velocity, $667 \pm 14 \text{ km s}^{-1}$. In order to assess the significance of the line broadening, we compared the line widths with a reference source, TW Hya. We know from previous work that TW Hya, compared to the “Rosetta stone” Capella, does not show line broadening exceeding the instrumental width of the line (Brickhouse et al. 2010). We thus found that the width of the lines in both HEG and MEG is larger than instrumental.

The blueshift, however, does not necessarily imply a velocity in a direction away from us. As in the previous outburst of RS Oph (Nelson et al. 2008; Drake et al. 2009), and in two other symbiotic recurrent novae (Drake et al. 2016; Orio et al. 2020), the line profiles are asymmetric and skewed toward the blue. This is likely to result in an apparent blueshift velocity when fitting the lines with Gaussians or other symmetric profiles, and it may be due only to intrinsic differential absorption in the nova ejecta, which is greater in the material receding from us than in the material moving toward us. Figure 4 illustrates the profiles of the H-like lines of Si XIV and Mg XII. In general, lines at longer wavelength, originating mostly in plasma at lower temperature because they are formed with a lower ionization potential, appear to be more skewed. We show in the

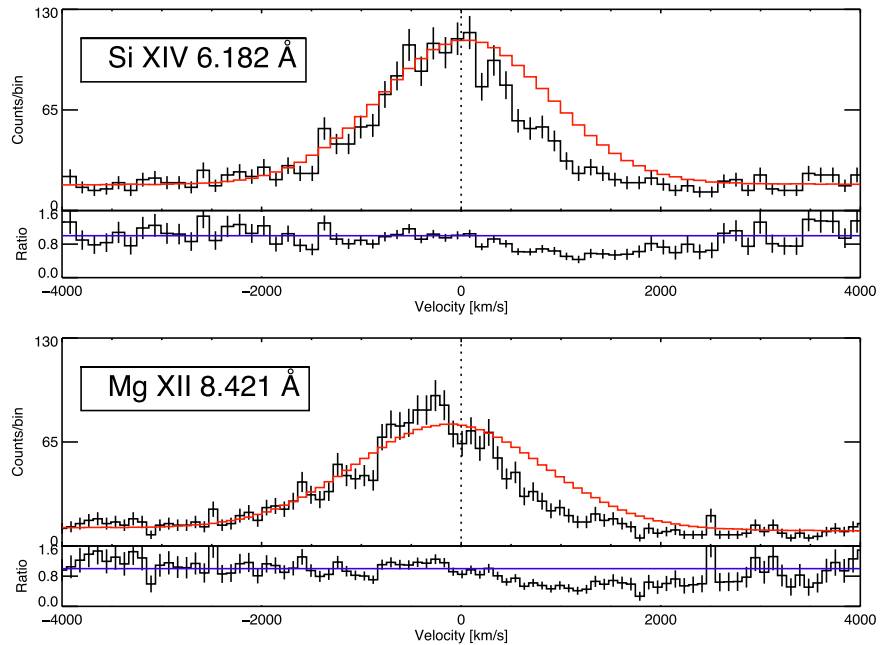


Figure 4. HEG line profiles of the H-like lines of Si XIV and Mg XII and fit with a Gaussian, in velocity space. The profile is clearly asymmetric; we interpret this as the effect of differential photoelectric absorption by the outflowing material of the nova, which erodes the red wing much more than the blue one.

next section that three days later this effect was quite evident, having observed and measured well lines in a “softer” range.

From the fit in Table 1 we have values of the emission measure (assuming a distance of 2.4 kpc). We know that the outflow is mainly in the equatorial plane and from the poles, and that the filling factor is low, but with the simplistic assumption that all the volume was filled in 18 days by material outflowing at 3500 km s^{-1} and adding the emission measures of the two components, we obtain an average value of the electron density of $6.96 \times 10^6 \text{ cm}^{-3}$ for the second model and $8.67 \times 10^6 \text{ cm}^{-3}$ for the first. However, the electron density in novae at this stage is likely to be higher, around 10^9 cm^{-3} (e.g., Neff et al. 1978). The average value obtained from the emission measure is often much lower because of clumping and low filling factor (see discussion by Orio et al. 2020). Low filling factors, in the 10^{-5} – 10^{-3} range, are often found also when analyzing optical spectra (e.g., Snijders et al. 1984; Andreae et al. 1991).

The $R = f/i$ ratio obtained from the HETG is 1.86 ± 0.31 for S XV, 4.32 ± 0.09 for Si XIII, and 1.68 ± 0.12 for Mg XI. These ratios can be compared with Figure 6 in Orio et al. (2020), showing the f ratio as a function of density in the absence of strong photoexcitation in three models in the literature. From this comparison, we find that the R values estimated for S XV and Si XIII do not constrain the electron density, but the value obtained for S XV gives an upper limit of about 10^{14} cm^{-3} . The value for Mg XI indicates about $3.16 \times 10^{12} \text{ cm}^{-3}$ and a lower limit of $2 \times 10^{13} \text{ cm}^{-3}$, which does indicate very significant clumping when compared with the average density obtained from the emission measure.

3. The XMM-Newton Observation

A second X-ray grating spectrum was obtained on 2021 August 30 in a 54 ks continuous XMM-Newton exposure starting at UT 15:45:41. The XMM-Newton observatory consists of five instruments behind three X-ray mirrors, plus an optical monitor (OM); all instruments observe

simultaneously. For this paper, we used the spectra of the Reflection Grating Spectrometers (RGS; den Herder et al. 2001), and we also examined the light curves of the EPIC pn and MOS cameras. The calibrated energy range of the EPIC cameras is 0.15–12 keV for the pn and 0.3–12 keV for the MOS. The RGS wavelength range is 5–38 Å, corresponding to the 0.33–2.5 keV energy range. We performed the data extraction and analysis with XMM-SAS (XMM Science Analysis System) version 19.1, see https://xmm-tools.cosmos.esa.int/external/xmm_user_support/documentation/sas_usg/USG.pdf. We extracted the RGS first-order spectra with the XMM-SAS task `rgsproc` and combined the RGS1 and RGS2 spectra with the `RGSCOMBINE` task. Periods of high background were rejected. The total count rate was $2.446 \pm 0.005 \text{ counts s}^{-1}$, and the total integrated flux we measured was $1.535 \times 10^{-10} \text{ erg cm}^{-2} \text{ s}^{-1}$.

Figure 5 shows a comparison between the Chandra spectrum of 2021 August 27 and the XMM-Newton spectrum obtained three days later in the 5–14 Å range in which the sensitivity is best matched. We observed a softening of the spectrum, with moderately decreased flux in lines formed at higher energy and increased flux in lines formed at lower energy. As the EPIC-pn light curve in Figure 6 and the RGS light curve in the lower panel in the bottom plot on the right in Figure 7 show, there was moderate variability with some decrease in count rate over 52 ks of “clean” observation. Particularly notable was a reduced flux in lines of oxygen, nitrogen, and carbon between 18 and 35 Å. Thus, we fitted the spectra of two separate intervals, indicated in blue and in orange in Figure 7. Strong lines are also marked for the first spectrum, and the many transitions are indicated in the bottom panel. In the first time interval, the total count rate was $2.514 \pm 0.008 \text{ counts s}^{-1}$, with an integrated flux of $1.584 \times 10^{-10} \text{ erg cm}^{-2} \text{ s}^{-1}$. In the second interval the total count rate in the 5–35 Å wavelength range was $2.395 \pm 0.009 \text{ counts s}^{-1}$, with an integrated flux of $1.508 \times 10^{-10} \text{ erg cm}^{-2} \text{ s}^{-1}$.

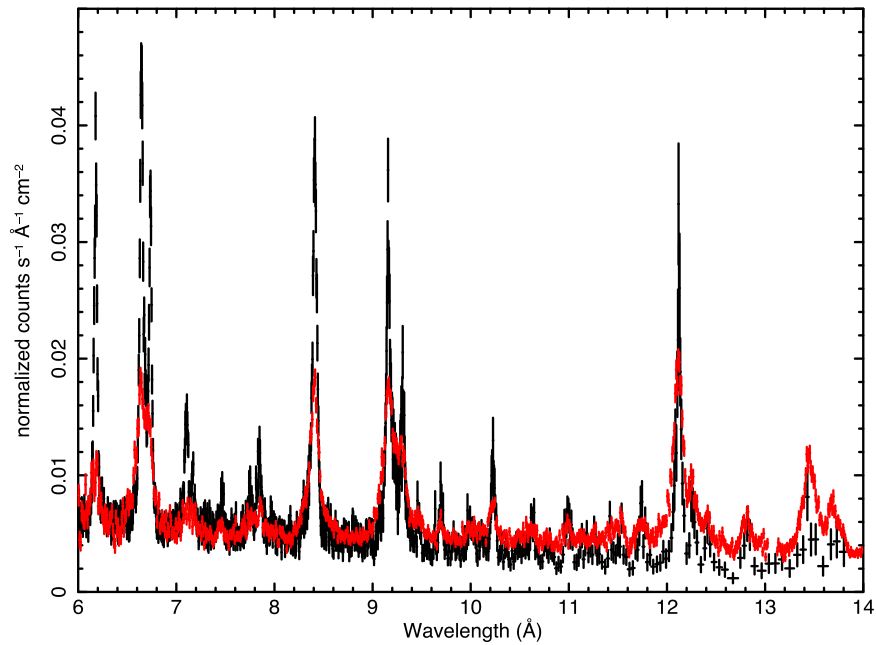


Figure 5. Comparison of the Chandra MEG spectrum (in black) observed on 2021 August 27 and the XMM-Newton RGS spectrum (in red) observed on 2021 August 30–31 in the 5–14 Å wavelength range.

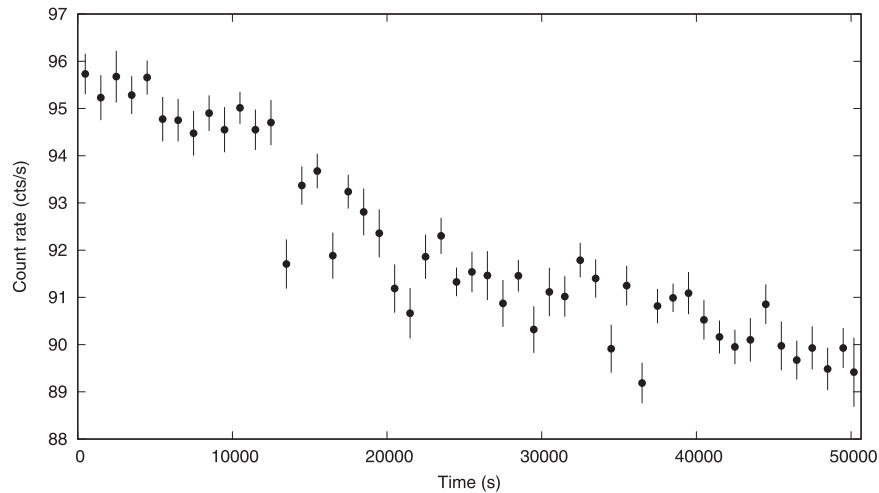


Figure 6. The 0.15–10 keV light curve measured with EPIC pn, binned with bins of 1000 s.

We note that the G -ratios of the spectrum integrated over the whole spectrum are only around 1 for Si XIII and Mg XI (consistent with collisional ionization equilibrium), while the R -ratios for these two triplets, respectively, are 4.02 ± 0.22 and 2.05 ± 0.49 , the latter implying an electron density $n_e \leq 10^{12} \text{ cm}^{-3}$, which is consistent with the HETG result.

3.1. Model Fitting

Table 3 shows the parameters of the fit to the spectra, observed in the two time intervals. At first, we performed the fit with two plasma component as for the Chandra fit above. Such fits can be obtained with two BVAPEC components at $\simeq 0.1 \text{ keV}$ and $\simeq 0.7 \text{ keV}$, respectively, yielding a value of $\chi^2/\text{d.o.f.}$ of 1.3. However, the fit to the spectra with two components does not match the EPIC broadband spectra, which show a broad iron feature at $\simeq 6.7 \text{ keV}$ (see Figure 8) and require a third component at higher temperature. The EPIC instruments cover a larger energy range than the RGS

(0.15–12 keV for the pn and 0.3–12 keV for the two MOS), and fitting their spectra requires a thermal component in the 2.0–2.5 keV range, close to what we found for the HETG spectrum of three days earlier.

A joint fit with any of the three EPIC instruments could only be obtained with $\chi^2 \geq 2.0$: the simultaneous fit could not be done more rigorously, and we assume that this is mainly because of the variability during the exposure. Moreover, we also have to factor in the fact that, in order to avoid possible pile-up and allow better timing studies, the EPIC pn and MOS-1 exposures were done with the small window and the EPIC MOS-2 in timing mode, not allowing a subtraction of a simultaneously observed background. However, to obtain a consistent result we fitted also the RGS spectra (separately) with an additional component at a fixed plasma temperature of 2.4 keV, which appears to be necessary to fit the EPIC spectra and contributes to flux also in the RGS energy range. The spectrum of the second time interval has lower flux at low

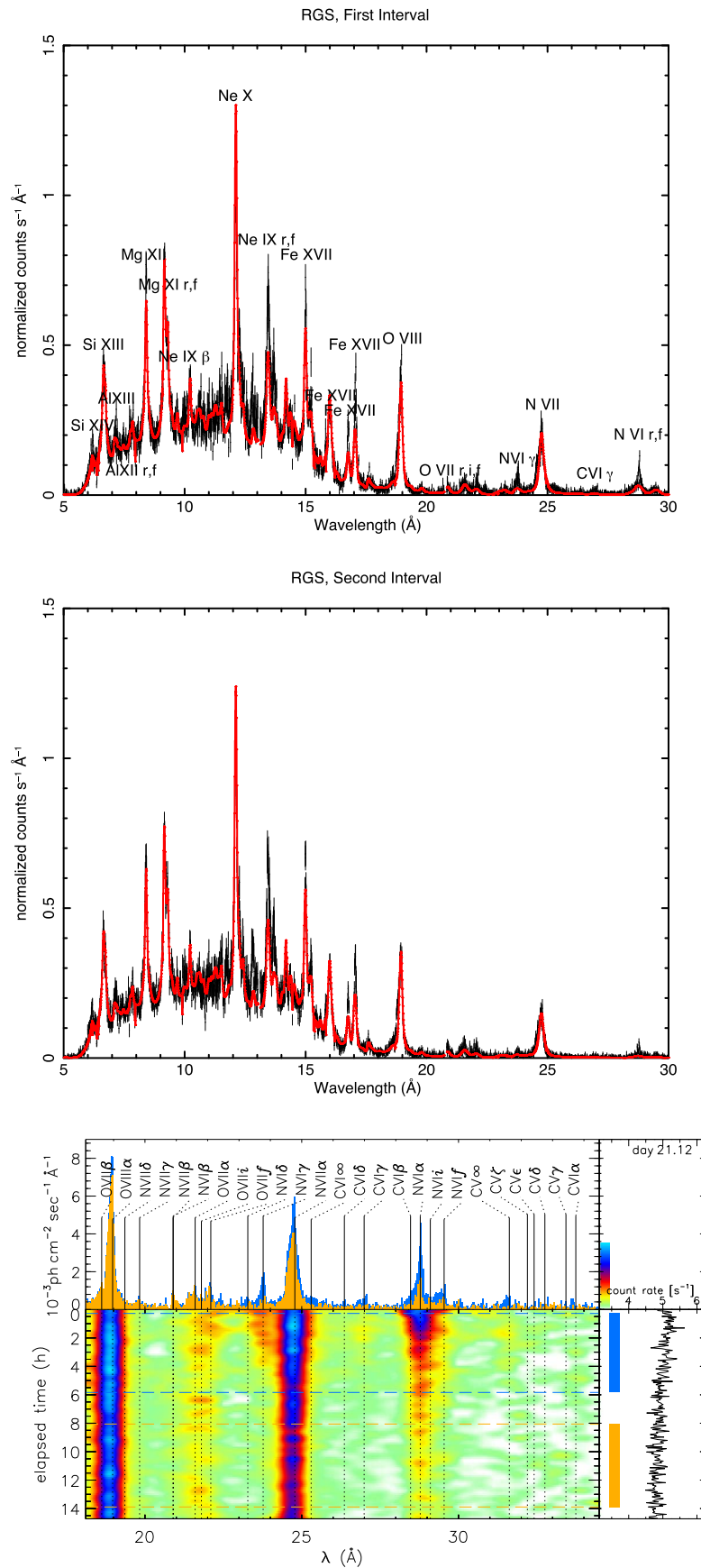


Figure 7. The spectra in the top and middle panels were extracted from the time intervals marked in the blue and orange intervals, respectively, in the light curve in the lower right part of the bottom panel. The upper left part of this bottom panel shows the comparison between the soft spectra in the blue and orange intervals, while the lower left part shows the variation in time with the color map shown in the upper right part. The red solid lines are the models in the first column of Table 2 for the first interval, and the model in the third column of Table 2 for the second interval.

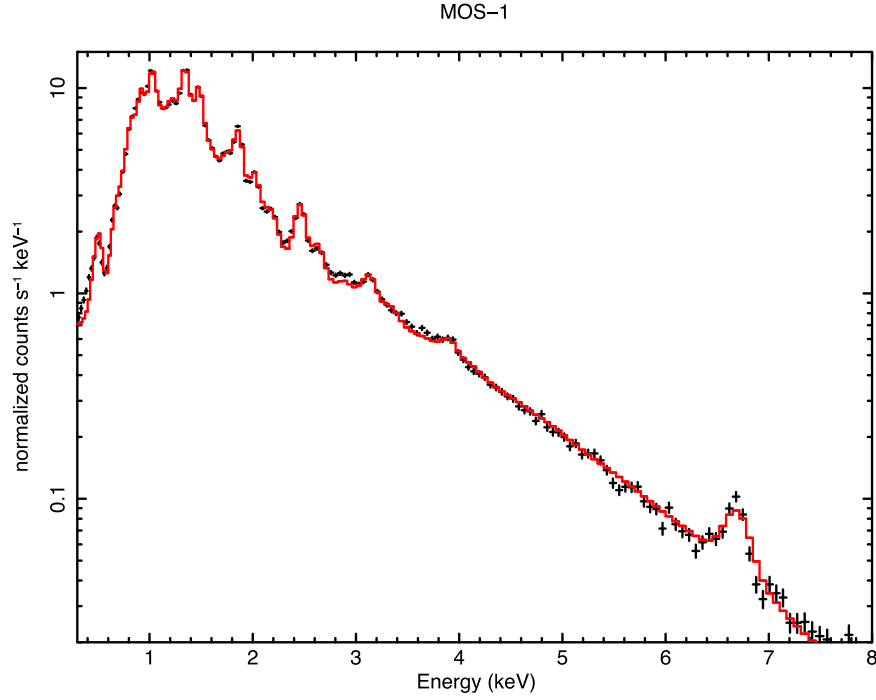


Figure 8. The averaged MOS-1 spectrum over the whole XMM-Newton exposure, on a logarithmic scale, and in red a model with three thermal components like the one in Table 3. The iron feature at $\simeq 6.7$ keV is detected with low count rate, but it is clearly present during the whole exposure time, and indicates the presence of the hottest component, even if its flux has decreased since day 18.

Table 3
Parameters for the Two RGS Fits Described in the Text for the August 30 Observation (on Day 21 after Optical Maximum) Split into Two Intervals

| | Interval 1 | Interval 2 |
|---|------------------------------------|------------------------------------|
| $\chi^2/\text{d.o.f.}$ | 1.8 | 1.6 |
| $N(\text{H})_{1,3} \times 10^{21} \text{ cm}^{-2}$ | 6.1 ± 1.3 | 6.4 ± 1.0 |
| $N(\text{H})_2 \times 10^{21} \text{ cm}^{-2}$ | 4.6 ± 0.2 | 4.6 (fixed) |
| kT_1 (eV) | 91 ± 19 | 128^{+300}_{-8} |
| kT_2 (keV) | 0.64 ± 0.06 | 0.64 ± 0.01 |
| kT_3 (keV) | 2.4 (fixed) | 2.4 (fixed) |
| $\text{EM}_1 \times (d(\text{kpc})/2.4)^2$ | $(1.298 \pm 0.24) \times 10^{57}$ | $(1.263 \pm 0.125) \times 10^{57}$ |
| $\text{EM}_2 \times (d(\text{kpc})/2.4)^2$ | $(1.056 \pm 0.11) \times 10^{58}$ | $(1.510 \pm 0.17) \times 10^{57}$ |
| $\text{EM}_3 \times (d(\text{kpc})/2.4)^2$ | $(5.267 \pm 0.682) \times 10^{57}$ | $(4.865 \pm 0.681) \times 10^{57}$ |
| F_a ($10^{-10} \text{ erg cm}^{-2} \text{ s}^{-1}$) | 1.52 ± 0.26 | 1.39 ± 0.18 |
| $F_{a,1}$ ($10^{-12} \text{ erg cm}^{-2} \text{ s}^{-1}$) | $2.97^{+1.17}_{-0.86}$ | 1.75 ± 0.28 |
| $F_{a,2}$ ($10^{-11} \text{ erg cm}^{-2} \text{ s}^{-1}$) | 10.40 ± 1.38 | 9.96 ± 1.15 |
| $F_{a,3}$ ($10^{-11} \text{ erg cm}^{-2} \text{ s}^{-1}$) | 4.51 ± 0.58 | 3.79 ± 0.53 |
| F_u ($10^{-10} \text{ erg cm}^{-2} \text{ s}^{-1}$) | 6.38 | 7.49 |
| C/C_\odot | $7.95^{+3.06}_{-2.56}$ | 0.1 (min.) |
| N/N_\odot | $40.2^{+6.6}_{-5.3}$ | 23 ± 3 |
| O/O_\odot | $2.97^{+0.43}_{-0.35}$ | $2.27^{+0.22}_{-0.20}$ |
| $\text{Ne}/\text{Ne}_\odot$ | $2.18^{+0.35}_{-0.25}$ | $1.49^{+0.15}_{-0.14}$ |
| $\text{Mg}/\text{Mg}_\odot$ | $2.34^{+0.32}_{-0.26}$ | $1.62^{+0.16}_{-0.14}$ |
| $\text{Al}/\text{Al}_\odot$ | $2.37^{+0.65}_{-0.58}$ | 1.56 ± 0.39 |
| $\text{Si}/\text{Si}_\odot$ | $1.86^{+0.25}_{-0.20}$ | 1.27 ± 0.12 |
| $\text{Fe}/\text{Fe}_\odot$ | 0.45 ± 0.06 | 0.35 ± 0.03 |
| v_{bs} (km s^{-1}) | 474 ± 24 | 525 ± 24 |
| $v_{\text{br},1}$ (km s^{-1}) | 1473^{+144}_{-137} | 1505^{+148}_{-153} |
| $v_{\text{br},2}$ (km s^{-1}) | 759 ± 36 | 734 ± 35 |
| $v_{\text{br},3}$ (km s^{-1}) | 2125^{+324}_{-327} | 2040^{+327}_{-297} |

Note. Both fits include three BVAPEC component. The parameters have the same meaning as in Table 1. Only the abundances that differ from solar within the statistical uncertainty are given. We assumed there are two different values of $N(\text{H})$ and broadening velocity for each component.

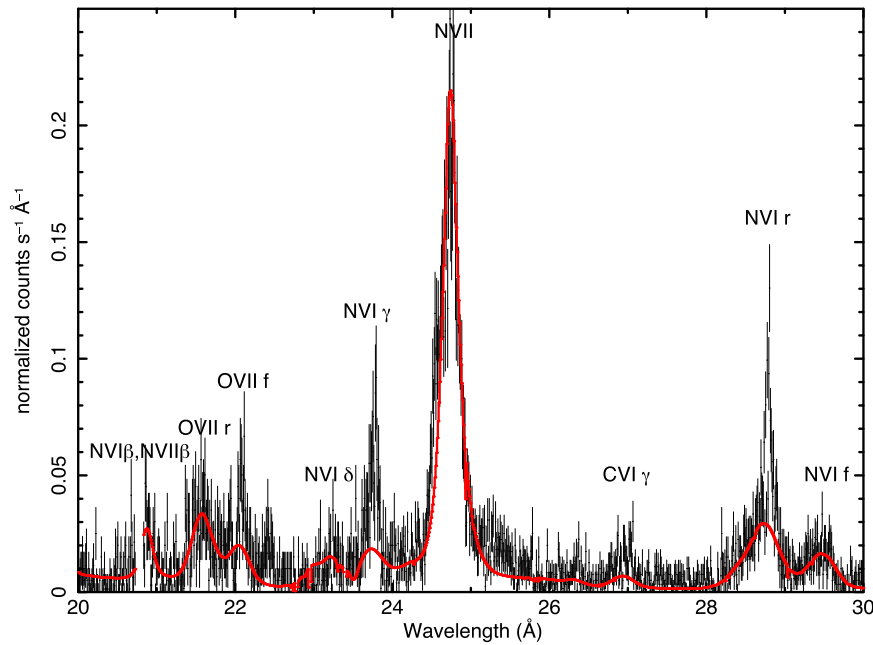


Figure 9. The spectra of the first interval in the 20–30 Å range, and the fit with the model in Table 3 (red solid lines). The third component at lower temperature is necessary for the fit in this range, but it was not evident in the higher HETG energy range three days earlier.

energy, so by using three components the uncertainty on the one at lower temperature became very large, thus we also fixed the value at a maximum of 130 eV, consistently with EPIC pn. We also “froze” one of the two values of $N(\text{H})$ to what we found for the first interval, $N(\text{H}) = 4.6 \times 10^{21} \text{ cm}^{-2}$. These fits yield a larger χ^2 than the ones with only two components, but qualitatively the single emission lines are better fitted. Partly because of the sensitivity of the RGS to a softer portion of the spectrum, and partly because of what appears to be actual cooling of the plasma within three days, we found it necessary to increase the number of free parameters when measuring more lines at longer wavelengths. We assumed that at least two components were absorbed differently, and the component at intermediate temperature has a different $N(\text{H})$ parameter. This is inspired by detailed hydrodynamical calculations (Orlando et al. 2009), which indicate that shocked ejecta and shocked circumstellar medium can have distinctly different temperatures and intrinsic absorption. We also assumed that the components have different velocity and thus contribute differently to line broadening. The apparent blueshift was small, so we left it fixed for all components. The model fits are not perfect: in fact the value of the $\chi^2/\text{d.o.f.}$ parameter for the best fit is only 1.8 in the first interval and 1.6 in the second, and the total flux is underestimated by 7%–8% relative to the actual measurement. These RGS model fits are shown with red solid lines in Figure 7, and Figure 9 presents the fit to the softest portion of the RGS spectrum. In addition, Figure 8 shows how the EPIC-MOS spectrum is fitted with the same composite model. Although also some of the L-shell lines of iron in the RGS are modeled with insufficient flux, we attribute the imperfect fit mainly to lines that we could not fit longward of 20 Å, shown in Figure 9: the flux of the N VI γ line, for example, is largely underestimated, the O VII He-like triplet is not well fitted (most notably the G -ratio is larger than in other He-like triplets, with a prominent forbidden line), and we also could not fit well the N VI He-like r line and a C VI γ line. We attribute this to a complexity that may require different abundances for the three

components, but we did not want to introduce a very large number of free parameters, since the fit to a high-resolution spectrum with “simple” physical models gives important indications, but more accurate results may require detailed hydrodynamical models.

3.2. Line Fluxes and Line Profiles

Table 2 reports also the wavelength, broadening velocity, and flux measured for the RGS, with the same Gaussian fits as used for the HETG. Like in the HETG case, the G -ratio (1.68 ± 0.52 for Mg XI, 1.15 for Si XIII) indicates a thermal plasma in collisional ionization equilibrium, without contribution of photoionization.

The lower energy range of the RGS, and most likely also the fact that the ejecta have already expanded a bit more, allows us to assess that the blueshift effect is mainly due to differential absorption, as we see in Figure 10. Note that the fit to this O VIII line is not included in Table 2, because we found it differed too much from a Gaussian profile.

4. Comparison with 2006 Observations

Chandra HETG spectra were obtained in 2006 earlier in the outburst, with the exposure starting 13.81 days after the outburst, about a week earlier than in 2021. The count rates were $2.950 \pm 0.024 \text{ counts s}^{-1}$ in the HEG and $1.271 \pm 0.014 \text{ counts s}^{-1}$ in the MEG, and the total flux was significantly higher than in 2021 on day 20: $3.3 \times 10^{-10} \text{ erg s}^{-1} \text{ cm}^{-2}$ measured with the MEG and $4.1 \times 10^{-10} \text{ erg s}^{-1} \text{ cm}^{-2}$ with the HEG. Figure 11 shows these spectra and a fit with the same model adopted for 2021. A comparison of the two spectra shows that the continuum in 2006 was higher and the emission lines were stronger, but the same lines were observed. The Fe XXV line at 1.778 Å was stronger than other lines, indicating a higher plasma temperature. Nelson et al. (2008) fitted the spectrum together with one from the RGS observed on the same day, reaching longer wavelengths, and obtained an

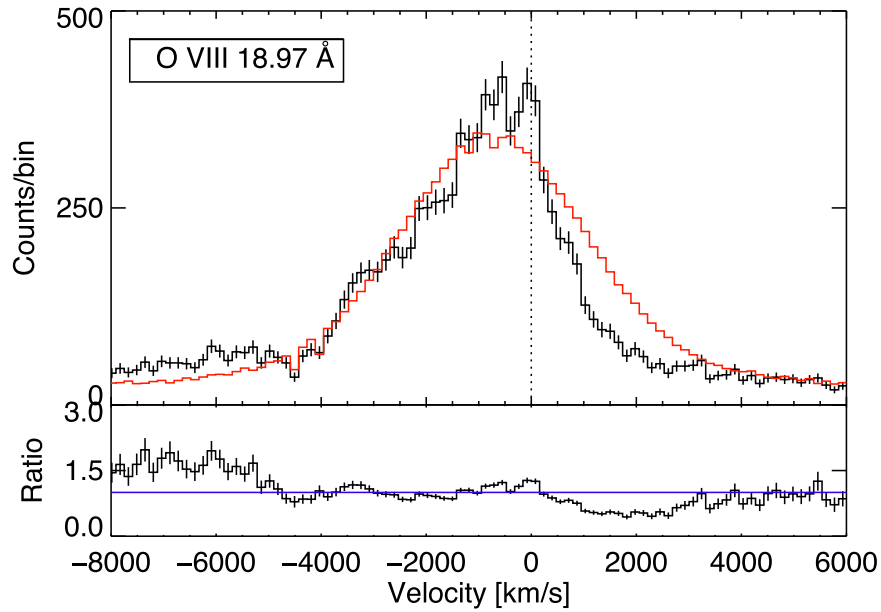


Figure 10. The O VIII H-like line observed with the RGS, shown in velocity space with 0 at rest wavelength of 18.9761 Å, and the fit with a Gaussian. The asymmetry, which we attribute to differential absorption in the receding outflow and in the one toward us, is more evident for lines with low ionization potential.

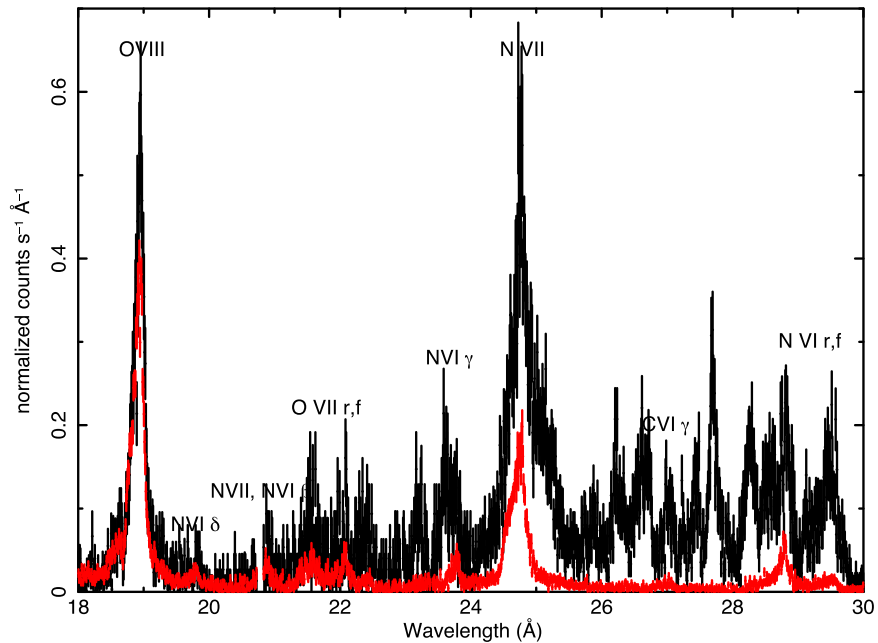


Figure 11. The RGS spectrum measured on 2006 March 10, 26 days after the optical maximum, is plotted in black and compared in the 20–30 Å range with the RGS spectrum observed on 2021 August 30, 21 days after the optical maximum, plotted in red.

optimal fit with four thermal plasma components at different temperature, 16.84, 2.31, 0.92, and 0.64 keV and $N(\text{H}) = 1.2 \times 10^{22} \text{ cm}^{-2}$. However, we find that with only two components of APEC plasma at 4.84 keV and 0.76 keV, respectively, and $N(\text{H}) = 5.6 \times 10^{21} \text{ cm}^{-2}$, we can fit the 2006 HEG and MEG spectra in the 1.2–15 keV range with a reduced $\chi^2 = 1.18$. Most of the emission lines are well fitted, although in the soft range some flux is underestimated. This fit indicates that most abundances are slightly enhanced with respect to solar, except that of iron, which turns out to be only about half of the solar value, like in 2021, probably indicating mixing with the red giant wind.

Next, we examined the 2006 RGS spectrum observed in an exposure starting exactly 26.13 days after maximum, to compare it with our 2021 RGS spectrum observed on day 21. We re-examined the flare claimed by Nelson et al. (2008), shown in their EPIC-pn light curve of the timing-mode exposure. We compared the light curve measured with the RGS gratings with that of an event file accumulated only from the exterior part of the EPIC-MOS-2 camera, without collecting photons from the source, to analyze the background, and found that the variability observed in the RGS and EPIC-pn was due to a background flare, and cannot be attributed to the source. We “cleaned” the 2006 March spectrum by excluding intervals

of high background: the “new lines” are not appearing suddenly during the exposure, but are always present when examining only intervals in which the background flare is excluded. We combined the RGS1 and RGS2 count rates of the first order, measuring a count rate of 2.819 ± 0.014 counts s^{-1} , only a little higher than in 2021. While the spectrum below 20 Å is a little more luminous and the line ratios are almost the same, Figure 11 shows that instead the spectrum in the 20–30 Å region differs considerably. Most of the unidentified lines of 2006 are not present in the 2021 spectrum, but we note two important facts: (a) the common features are identified without assuming a large blueshift for the 2006 spectrum (a blueshift velocity of 8000 km s^{-1} was proposed by Nelson et al. (2008) in order to identify some of the lines); (b) the emission lines that are not common to the 2021 spectrum presented here did indeed appear in 2021 some time later in the outburst, in a spectrum measured in 2021 with the RGS about two weeks later, and will be described in a paper led by coauthor J. U. Ness (in preparation).

5. Discussion

The high-spectral-resolution spectra we obtained cover relatively narrow ranges, but they are rich in many emission lines that constrain the plasma temperatures. Adding information obtained in broadband in wider energy ranges (with NICER less than a day earlier for the HETG, and with the simultaneous EPIC spectra for the RGS), we were able to better constrain the value of the absorbing column density $N(H)$ and plasma temperatures and to some extent also the abundances, especially that of iron. The Swift XRT did not have the signal-to-noise ratio and spectral resolution to detect the emergence of a much softer component in an emission lines spectrum, which is instead evident in the XMM-Newton RGS spectrum. The plasma temperatures of two components estimated with the Swift XRT are in the same ballpark as measured with the gratings, but the Swift XRT fits miss the emergence of a much softer component at wavelengths longward of 23 Å, and this is evident in the XMM-Newton RGS spectrum. This component became important in the following evolution, because in broadband spectra it is easily confused with the emergence of the central supersoft source, generating confusion in estimating the amount of ejected mass and/or some crucial physical parameters.

We confirm that the high-resolution spectra reveal a very low filling factor of the ejecta and the effect of differential intrinsic absorption in the material flowing away from our line of sight and toward it. The iron abundance in the fits, driven mostly by the L-shell iron lines, is lower than solar, at most half the solar value, but possibly even quite lower. The RGS spectrum of day 21 indicates also high nitrogen abundance, possibly around 40 times solar in the spectrum of the first part of the exposure. This is consistent with the optical spectra of Pandey et al. (2022). It is thus likely that at this point CNO-processed ejected material was mixing with the circumstellar red giant wind. However, iron remained depleted. In the optical nebular spectrum of outburst day 201 after the 1985 outburst maximum, Contini et al. (1995) found 10 times enhanced nitrogen, the ratio of carbon to nitrogen 100 times the solar value, and iron abundance only 17% of the solar value, so these results seem to be consistent throughout outburst cycles.

If we interpret the line broadening as due to the velocity of the emitting medium, it is interesting to note that on day 18 this

velocity is significantly lower than that derived in the optical spectra, but it appears to have increased on day 21 in the lines formed at lower and at higher energy. Aydi et al. (2020) noticed that in all optical spectra of novae a fast velocity component follows a slower one, and often there is evidence of two or more mass ejection episodes. The varying velocity estimates of the X-ray-emitting ejecta of RS Oph and the discrepancy with the maximum velocity observed in its optical spectra are consistent with this complex scenario and indicate that the shocked material is associated with the slower outflow episodes.

6. Conclusions

We can summarize the main conclusions as follows.

1. Assuming the distance estimate given by Rupen et al. (2008), the precisely measured flux on day 18 implies an X-ray luminosity of 1.738×10^{35} erg s^{-1} in the 0.4–10 keV range and 1.023×10^{35} erg s^{-1} in the 0.33–2.5 keV range on day 21. The best fits indicate absolute luminosity of about 3.9×10^{35} erg s^{-1} on day 18 and 5.2×10^{35} erg s^{-1} on day 21, confirming that shocks in the outflows of symbiotic novae produce very luminous X-ray sources.
2. 18 days after the optical maximum, the HETG X-ray high-resolution spectra of RS Oph in the 2021 outburst are fitted with a thermal plasma with at least two components at different temperatures. Observing in the lower energy range with the XMM-Newton RGS on day 21, we measured emission lines produced in a third thermal component, at about 0.1 keV. Although the HETG was not sensitive in the softest range, the NICER spectra in the 0.2–12 keV range on day 18 impose low flux limits on this soft component on day 19 (M. Orio et al. 2022, in preparation), so we suggest that this component was only emerging between the two dates of our observations, spaced three days apart. We anticipate that comparison with another XMM-Newton RGS spectrum obtained at a later outburst phase indicates that this soft thermal component appears to become more luminous with time between the third and fifth weeks after the outburst (J. U. Ness et al. 2022, in preparation).
3. An interesting parameter is the column density, proving intrinsic absorption of the ejecta. In fact, the interstellar column density was estimated to be $(2.4 \pm 0.6) \times 10^{21}$ cm^{-2} from H I absorption by Hjellming et al. (1986). However, the values obtained in our fits indicate much lower intrinsic “wind absorption” than estimated by Page et al. (2022) with the Swift data. On day 18, these authors estimate an additional $N(H)$ of $(1.50\text{--}1.54) \times 10^{22}$ cm^{-2} , which is so high as to be ruled out even by the fits to the HETG alone (without resorting to the NICER data). These authors also estimate a wind absorption still as high as $N(H) = 1.37 \times 10^{22}$ cm^{-2} on day 21, and conclude that the outflowing material had exactly the same characteristics in 2021. We would like to point out that it is difficult and not always reliable to draw firm conclusions only from the broadband data, while a combination of broadband and high-resolution X-ray spectra constrains the value of the column density much more accurately.

4. An important advantage of our high-resolution spectra is the precise determination of the absorbed flux. This cannot be done with broadband spectra, which rely on modeling to give a flux estimate. The flux measured with the XMM-Newton RGS on day 26 after the 2006 outburst maximum was 1.6×10^{-10} erg cm⁻² s⁻¹, still a little higher than what we measured earlier in post-outburst phase, on day 21 in 2021. Most likely, this indicates faster cooling of the plasma in the 2021 outburst. The indications of lower intrinsic absorption and more rapidly decreasing flux in 2021 compared to the 2006 data of Nelson et al. (2008) indicate that the ejected mass was larger in 2006.
5. Another very important caveat is derived by the comparison with the γ -ray emission in the 0.2–5 GeV range of the Fermi-LAT (Cheung et al. 2022). Around day 20 post-optical maximum, the flux measured with Fermi was about 10^{-7} erg cm⁻² s⁻¹. With the gratings in the X-ray range, we are able to measure the X-ray flux precisely, and on day 18 we only measured 2.6×10^{-10} erg cm⁻² s⁻¹ in the 0.5–10 keV range (see the Chandra data), three orders of magnitude less than in the Fermi range. Not only does the shock energy loss by particles appear to exceed the X-ray emission from the hot gas by such a large amount, but also the plasma temperature of the detectable emission is much lower than predicted by Vurm & Metzger (2018), constraining the models of γ -ray emission and most likely implying that the site of the shocks we observed is *not* the same as the site of the shock whose consequences were observed with Fermi. The proposed explanation for the absence of simultaneous γ -ray and X-ray flux consistent with each other in several papers is that the X-rays associated with the γ -ray flux are affected by too high absorption to be detected (e.g., Vurm & Metzger 2018), but our spectra rule out such high column density. This result is new and important, because only during the RS Oph outburst were γ -ray and X-ray flux measured simultaneously in a nova.
6. The only abundances that are quite clearly constrained are those of nitrogen (enhanced with respect to solar values) and of iron (which is depleted), consistently with results inferred after a previous outburst (Contini et al. 1995). However, there is some evidence that the abundances in the two components may not be the same, and most elements, except iron, may be enhanced in the less cool component, and closer to solar values in the hotter one. Moreover, the fit on day 19 can be obtained with abundances that are close to solar, while on day 22 a better fit is obtained with enhanced values, perhaps indicating ongoing mixing with the ejecta (there are, however, quite large uncertainties). The spectrum on day 21 is better fitted with different absorbing column density for the two components, with values that are still significantly higher than the interstellar value, although only about half of the estimate of Page et al. (2022).
7. We also note that on day 21, we did not measure yet many of the—partially unidentified—emission lines in the soft range measured on day 26 of the outburst in 2006. During this XMM-Newton exposure, we also observed a decrease in count rate, due mainly to decreasing flux in the emission lines in the soft region.

Separate fits to the spectrum observed in the first part of the day 21 exposure and in the second half are more consistent with variable flux of the softer component than with variable absorption in the ejecta. However, we anticipate that the emission lines in this region later on in the outburst become stronger, more lines were measurable, and the flux of the softer component increased: this development is described in papers describing subsequent exposures with the RGS gratings (J. U. Ness et al. 2022, in preparation) and with NICER (M. Orio et al. 2022, in preparation).

8. Finally, these data and their analysis, including the line profiles, the column density estimate, and the low velocity associated with the X-ray-emitting outflow, should allow us to refine sophisticated models of the dynamics of the ejecta like those of Orlando et al. (2009) for the 2006 outburst.


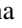





A second article with other high-spectral-resolution X-ray grating spectra of RS Oph is in the works, led by coauthor J. U. Ness, and will cover the initial emergence of the supersoft X-ray source.

M.O. acknowledges useful and interesting conversations with Joe Cassinelli and Tommy Nelson. The immediate comparison with the NICER data was possible thanks to Keith Gendreau. M.O. was supported by NASA and NASA-Smithsonian awards for research with XMM-Newton and Chandra, respectively. G.J.M.L. is a member of the CIC-CONICET (Argentina) and acknowledges support from grant ANPCYT-PICT 0901/2017. J.M. was financed by the Polish National Science Centre grant 2017/27/B/ST9/01940.

Facilities: Chandra—XMM-Newton

Software: CIAO v4.14.0 (Fruscione et al. 2006), XSPEC v6.30.6 (Arnaud 1996, 2022), GRPPHA (see Dorman & Arnaud 2001, and references therein), SAS v19.1 https://xmm-tools.cosmos.esa.int/external/xmm_user_support/documentation/sas_usg/USG.pdf.

ORCID iDs

Marina Orio  <https://orcid.org/0000-0003-1563-9803>
 E. Behar  <https://orcid.org/0000-0001-9735-4873>
 G. J. M. Luna  <https://orcid.org/0000-0002-2647-4373>
 J. J. Drake  <https://orcid.org/0000-0002-0210-2276>
 J. Gallagher  <https://orcid.org/0000-0001-8608-0408>
 J. S. Nichols  <https://orcid.org/0000-0003-3298-7455>
 J. U. Ness  <https://orcid.org/0000-0003-0440-7193>
 J. Mikolajewska  <https://orcid.org/0000-0003-3457-0020>
 M. Della Valle  <https://orcid.org/0000-0003-3142-5020>
 R. Ignace  <https://orcid.org/0000-0002-7204-5502>

References

- Acciari, V. A., Ansoldi, S., Antonelli, L. A., et al. 2022, *NatAs*, **6**, 689
 Andrae, J., Drechsel, H., Snijders, M. A. J., & Cassatella, A. 1991, *A&A*, **244**, 111
 Anupama, G. C., & Mikolajewska, J. 1999, *A&A*, **344**, 177
 Arnaud, K. 2022, *BAAS*, **54**, 2022n3i203p02
 Arnaud, K. A. 1996, in *ASP Conf. Ser. 101, Astronomical Data Analysis Software and Systems V*, ed. G. H. Jacoby & J. Barnes (San Francisco, CA: ASP), 17
 Aydi, E., Chomiuk, L., Izzo, L., et al. 2020, *ApJ*, **905**, 62
 Bailer-Jones, C. A. L., Rybizki, J., Fouesneau, M., Demleitner, M., & Andrae, R. 2021, *AJ*, **161**, 147

- Barry, R. K., Mukai, K., Sokoloski, J. L., et al. 2008, in ASP Conf. Ser. 401, RS Ophiuchi (2006) and the Recurrent Nova Phenomenon, ed. A. Evans et al. (San Francisco, CA: ASP), 52
- Bode, M. F. 1987, in Proc. Manchester Conf., RS Ophiuchi (1985) and the recurrent nova phenomenon, held at Manchester, UK, 16-18 December 1985 (Utrecht: VNU Science Press)
- Bode, M. F., O'Brien, T. J., Osborne, J. P., et al. 2006, *ApJ*, 652, 629
- Brandi, E., Quiroga, C., Mikolajewska, J., Ferrer, O. E., & Garca, L. G. 2009, *A&A*, 497, 815
- Brickhouse, N. S., Cranmer, S. R., Dupree, A. K., Luna, G. J. M., & Wolk, S. 2010, *ApJ*, 710, 1835
- Cheung, C. C., Johnson, T. J., Jean, P., et al. 2022, *ApJ*, 935, 44
- Contini, M., Orio, M., & Prialnik, D. 1995, *MNRAS*, 275, 195
- Dobrzycka, D., Kenyon, S. J., Proga, D., Mikolajewska, J., & Wade, R. A. 1996, *AJ*, 111, 2090
- Dorman, B., & Arnaud, K. A. 2001, in ASP Conf. Ser. 238, Astronomical Data Analysis Software and Systems X, ed. F. R. Harnden, Jr., F. A. Primini, & H. E. Payne (San Francisco, CA: ASP), 415
- Drake, J. J., Laming, J. M., Ness, J. U., et al. 2009, *ApJ*, 691, 418
- Drake, J. J., Delgado, L., Laming, J. M., et al. 2016, *ApJ*, 825, 95
- Ferrigno, C., Savchenko, V., Bozzo, E., et al. 2021, ATel, 14855, 1
- Fruscione, A., McDowell, J. C., Allen, G. E., et al. 2006, *Proc. SPIE*, 6270, 62701V
- H.E.S.S. Collaboration 2022, *Sci*, 376, 77
- Hachisu, I., Kato, M., & Luna, G. J. M. 2007, *ApJL*, 659, L153
- Hjellming, R. M., van Gorkom, J. H., Taylor, A. R., et al. 1986, *ApJL*, 305, L71
- Ignace, R. 2001, *ApJL*, 549, L119
- Luna, G. J. M., Carrera, R., Enoto, T., et al. 2021, ATel, 14873, 1
- Meng, X., Chen, X., & Han, Z. 2008, *A&A*, 487, 625
- Mikolajewska, J., Aydi, E., Buckley, D., Galan, C., & Orio, M. 2021, ATel, 14852, 1
- Mikolajewska, J., & Shara, M. M. 2017, *ApJ*, 847, 99
- Munari, U., & Valisa, P. 2021a, ATel, 14840, 1
- Munari, U., & Valisa, P. 2021b, arXiv:2109.01101
- Munari, U., Valisa, P., & Ochner, P. 2021, ATel, 14895, 1
- Neff, J. S., Smith, V. V., & Ketelsen, D. A. 1978, *ApJS*, 38, 89
- Nelson, T., Orio, M., Cassinelli, J. P., et al. 2008, *ApJ*, 673, 1067
- Ness, J. U., Starrfield, S., Beardmore, A. P., et al. 2007, *ApJ*, 665, 1334
- Ness, J. U., Drake, J. J., Starrfield, S., et al. 2009, *AJ*, 137, 3414
- Nikolov, Y., & Luna, G. J. M. 2021, ATel, 14863, 1
- Oegelman, H., Beuermann, K., & Krautter, J. 1984, *ApJL*, 287, L31
- Orio, M. 2012, *BASI*, 40, 333
- Orio, M., Drake, J. J., Ness, J. U., et al. 2020, *ApJ*, 895, 80
- Orlando, S., Drake, J. J., & Laming, J. M. 2009, *A&A*, 493, 1049
- Orlando, S., Drake, J. J., & Miceli, M. 2017, *MNRAS*, 464, 5003
- Osborne, J. P., Page, K. L., Beardmore, A. P., et al. 2011, *ApJ*, 727, 124
- Page, K. L., Beardmore, A. P., Osborne, J. P., et al. 2022, *MNRAS*, 514, 1557
- Pandey, R., Habtie, G. R., Bandyopadhyay, R., et al. 2022, *MNRAS*, 515, 4655
- Porquet, D., Dubau, J., & Grosso, N. 2010, *SSRv*, 157, 103
- Rupen, M. P., Mioduszewski, A. J., & Sokoloski, J. L. 2008, *ApJ*, 688, 559
- Schaefer, B. E. 2004, IAU Circ., 8396, 2
- Shidatsu, M., Negoro, H., Mihara, T., et al. 2021, ATel, 14846, 1
- Shore, S. N., Teyssier, F., & Thizy, O. 2021, ATel, 14881, 1
- Snijders, M. A. J., Batt, T. J., Seaton, M. J., Blades, J. C., & Morton, D. C. 1984, *MNRAS*, 211, 7P
- Sokoloski, J. L., Luna, G. J. M., Mukai, K., & Kenyon, S. J. 2006, *Natur*, 442, 276
- Starrfield, S., Timmes, F. X., Iliadis, C., et al. 2012, *BaltA*, 21, 76
- Vurm, I., & Metzger, B. D. 2018, *ApJ*, 852, 62
- Wagner, S. J. & H.E.S.S. Collaboration 2021a, ATel, 14844, 1
- Wagner, S. J. & H.E.S.S. Collaboration 2021b, ATel, 14857, 1
- Wolf, W. M., Bildsten, L., Brooks, J., & Paxton, B. 2013, *ApJ*, 777, 136
- Yaron, O., Prialnik, D., Shara, M. M., & Kovetz, A. 2005, *ApJ*, 623, 398